ON THE ORIGIN OF THE SOLAR MORETON WAVE OF 2006 DECEMBER 6

K. S. Balasubramaniam[1], E. W. Cliver[2], A. Pevtsov[3], M. Temmer[4], T. W. Henry[3], H. S. Hudson[5], S. Imada[6], A. G. Ling[7], R. L. Moore[8], N. Muhr[4], D. F. Neidig[3,12], G. J. D. Petrie[9], A. M. Veronig[4], B. Vršnak[10], and S. M. White[11]

[1] Space Vehicles Directorate, Air Force Research Laboratory, Sunspot, NM 88349, USA
[2] Space Vehicles Directorate, Air Force Research Laboratory, Hanscom AFB, MA 01731, USA
[3] National Solar Observatory, Sunspot, NM 88349, USA
[4] IGAM/Kanzelhöhe Observatory, Institute of Physics, Universität Graz, A-8010 Graz, Austria
[5] Space Sciences Laboratory, University of California, Berkeley, CA 94720, USA
[6] Institute of Space and Astronautical Science, Japan Aerospace Exploration Agency, Sagamihara, Kanagawa 229–8510, Japan
[7] Atmospheric Environmental Research Inc., Lexington, MA 02421, USA
[8] National Aeronautics and Space Administration, Marshall Space Flight Center, Huntsville, AL 35812, USA
[9] National Solar Observatory, Tucson, AZ 85719, USA
[10] Faculty of Geodesy, University of Zagreb, Hvar Observatory, HR 10000 Zagreb, Croatia
[11] Space Vehicles Directorate, Air Force Research Laboratory, Kirtland AFB, NM 87117, USA

ABSTRACT

We analyzed ground- and space-based observations of the eruptive flare (3B/X6.5) and associated Moreton wave ($\sim$850 km s^{-1}; $\sim$270° azimuthal span) of 2006 December 6 to determine the wave driver—either flare pressure pulse (blast) or coronal mass ejection (CME). Kinematic analysis favors a CME driver of the wave, despite key gaps in coronal data. The CME scenario has a less constrained/smoother velocity versus time profile than is the case for the flare hypothesis and requires an acceleration rate more in accord with observations. The CME picture is based, in part, on the assumption that a strong and impulsive magnetic field change observed by a GONG magnetograph during the rapid rise phase of the flare corresponds to the main acceleration phase of the CME. The Moreton wave evolution tracks the inferred eruption of an extended coronal arcade, overlying a region of weak magnetic field to the west of the principal flare in NOAA active region 10930. Observations of Hα foot point brightenings, disturbance contours in off-band Hα images, and He i 10830 Å flare ribbons trace the eruption from 18:42 to 18:44 UT as it progressed southwest along the arcade. *Hinode* EIS observations show strong blueshifts at foot points of this arcade during the post-eruption phase, indicating mass outflow. At 18:45 UT, the Moreton wave exhibited two separate arcs (one off each flank of the tip of the arcade) that merged and coalesced by 18:47 UT to form a single smooth wave front, having its maximum amplitude in the southwest direction. We suggest that the erupting arcade (i.e., CME) expanded laterally to drive a coronal shock responsible for the Moreton wave. We attribute a darkening in Hα from a region underlying the arcade to absorption by faint unresolved post-eruption loops.

Key words: Sun: activity – Sun: coronal mass ejections (CMEs) – Sun: flares

Online-only material: animations, color figure

1. INTRODUCTION

Moreton waves, large-scale waves observed in Hα emanating from the sites of major solar flares, were first reported 50 years ago (Moreton 1960, 1961, 1964; Moreton & Ramsey 1960; Athay & Moreton 1961; Dodson & Hedeman 1964; Ramsey & Smith 1966; Dodson & Hedeman 1968). Such waves have characteristic speeds of $\sim$1000 km s^{-1} and tend to be directional, with angular widths typically in the range from 60° to 150° (Smith & Harvey 1971; Warmuth et al. 2004a; Veronig et al. 2006), although cases with fragmented arcs collectively spanning larger angles have been reported (Pick et al. 2005; Balasubramaniam et al. 2007; Muhr et al. 2008, 2010). Following their discovery, the pre-eminent research result on these dramatic solar events was Uchida's synthesis (Uchida 1968, 1973, 1974a, 1974b; Uchida et al. 1973) of Moreton waves and metric type II radio bursts (Payne-Scott et al. 1947; Wild & McReady 1950) in terms of a flare-generated fast-mode MHD wave. The characteristic down–up pattern of Moreton waves indicates a depression of the chromosphere (or lower corona; Balasubramaniam et al. 2007) by a coronal shock and subsequent relaxation or restoration. Recently, Warmuth et al. (2004a)

have argued for a general synthesis of large-scale wave phenomena—including waves observed in soft X-rays (Khan & Aurass 2002; Narukage et al. 2002; Hudson et al. 2003; Warmuth et al. 2005), extreme ultra-violet (EIT or EUV waves; Neupert 1989; Thompson et al. 1998, 1999), He i 10830 Å (Vršnak et al. 2002; Gilbert & Holzer 2004), microwaves (Warmuth et al. 2004a; White & Thompson 2005), as well as Moreton waves and type II radio bursts. Warmuth et al. (2004b) noted that the amplitude decay, perturbation profile broadening, and deceleration they observed in a sample of 12 large-scale waves were all consistent with Uchida's picture of a freely propagating fast-mode shock. We refer the reader to Vršnak (2005) for a general discussion of large-scale wave terminology.

Amongst the large-scale waves, Zhukov & Auchère (2004) have suggested two types or modes of propagating EIT disturbances—a true wave mode and an eruptive mode associated with restructuring following a coronal mass ejection (CME). Aspects of this nascent bi-modal picture have been put forth by a number of researchers (Delannée & Aulanier 1999; Delannée 2000; Biesecker et al. 2002; Chen et al. 2002, 2005; Chen 2009; Harra & Sterling 2003; Attrill et al. 2007, 2009; Delannée et al. 2008; Wang et al. 2009; Zhukov et al. 2009; Cohen et al. 2009; Wills-Davey & Attrill 2009; Ma et al. 2009; Dai et al. 2010;

---
[12] Emeritus.

and Yang & Chen 2010). The view that some EIT waves are "pseudo-waves" has prompted a reaction—several recent papers based on high-cadence *STEREO* observations (Long et al. 2008; Veronig et al. 2008; Gopalswamy et al. 2009a; Patsourakos & Vourlidas 2009; Patsourakos et al. 2009; Kienreich et al. 2009; Veronig et al., 2010) show that other traveling EIT disturbances definitely are freely propagating MHD waves.

The origin of large-scale waves has been vigorously debated during the last decade, sparked by the observations of EIT waves (Thompson et al. 1998, 1999) and the coincident rekindling of research on the nature of metric type II bursts (Gopalswamy et al. 1998, 1999; Cliver 1999; Cliver et al. 1999). Recent reviews have summarized the current understanding:

1. Warmuth (2007): "The causes of coronal waves are still unclear. In principle, flares, small-scale ejecta, and CMEs are viable mechanisms for the generation of large-amplitude disturbances, while large-scale eruptions such as CMEs seem to be the necessary ingredient within the framework of a magnetic reconnection scenario. Careful multiwavelength observations of individual events as well as statistical studies will be needed to resolve this issue."

2. Vršnak & Cliver (2008): "... the existence of CME-generated type II bursts is not in question. It is generally accepted that all interplanetary (kilometric) type IIs (Sheeley et al. 1985; Cane et al. 1987), many (if not all) decametric-hectometric type IIs (Gopalswamy et al. 2000), and at least some metric type II bursts (e.g., Raymond et al. 2000; Cane & Erickson 2005) are CME-generated. On the other hand, the existence of "pure" flare-generated type II bursts remains to be demonstrated."

Vršnak & Cliver (2008) proposed two lines of research, both involving imaging observations of type II bursts, to provide insight on the relative importance of flare and CME generation mechanisms for large-scale waves. This problem may also be addressed by investigating Moreton waves which are observed at a much higher spatial resolution and with much better image fidelity than type II bursts. On the other hand, Moreton waves are only infrequently reported compared with type II bursts, due to both observing/reporting practices, and their weaker signal-to-noise ratios. For example, during solar cycle 23 (1997–2006), only ~30 Moreton waves were reported (Warmuth 2010) versus ~1000 metric type II bursts, and of these ~30 Moreton waves, only the 2006 December 6 event exhibited a contiguous span ~270°. For this event, the occurrence of a major eruption on the approach to solar minimum resulted in a broad, long-lasting wave that was relatively unimpeded by other active regions (ARs) during its passage across the disk.

Recently, Temmer et al. (2009) used an analytic model for the 2005 January 17 eruption to deduce that the associated Moreton wave was more likely driven by either an expanding flare volume or by a lateral motion of the CME flanks (piston-driven shock scenario) than by an upward motion of the CME front (bow shock). As Vršnak & Cliver (2008) noted: "... during the impulsive phase, it is sometimes difficult to disentangle flare motions from CME motions, i.e., to distinguish between "flare expansion" and "CME." However, it is clear that both the CME expansion towards the high corona and the nonthermal/thermal energy release beneath the CME are present, representing two physically different aspects of the eruption. ... The root of the "flare versus CME" controversy lies in the MHD equation of motion, containing two different terms: the Lorentz force (driver of the CME) and the pressure gradient (presumably driving the expansion of hot flare plasma). ... In both cases the wave is formed by magnetoplasma motion perpendicular to the magnetic field that could be considered as a 3-dimensional piston."

In this study we explore these two possible wave drivers—flare volume expansion and lateral CME motion—for the 2006 December 6 Moreton wave. Despite key gaps in coronal observations, this eruptive event was well observed in a number of wavelengths, providing the necessary tools to constrain the kinematics. Our analysis is presented in Section 2 and the results are summarized and discussed in Section 3.

2. ANALYSIS

2.1. Data Sources

The principal data for this study were Hα (centerline and ±0.4 Å) images obtained by the prototype ISOON patrol telescope (Neidig et al. 1998) located at the National Solar Observatory, Sacramento Peak. The ISOON telescope is a 25 cm polar axis refractor. The data consist of photometric quality (<5% uncertainty) images at selected wavelengths in a 2048 by 2048 pixel grid, for a nominal angular resolution of 1.1 arcsec. At present, Hα centerline and off-band images are made every minute (with centerline taken approximately on the minute and red and blue following, in turn, at 3–4 s intervals), a white-light image (WL) every 5 minutes, and a He I 10830 Å image every 10 minutes. Additional data were obtained from the Michelson–Doppler Investigation (MDI, magnetogram; Scherrer et al. 1995); the Global Oscillation Network Group (GONG, magnetic field changes; Harvey et al. 1988), the *Ramaty High-Energy Solar Spectroscopic Imager* (*RHESSI*, hard X-ray time profiles and images; Lin et al. 2002); the *Geostationary Orbiting Environmental Satellite* (*GOES*, 1–8 Å X-ray time profile); the *Transition Region and Coronal Explorer* (*TRACE*, images at 195 Å and 1600 Å; Handy et al. 1999); the EUV Imaging Spectrometer of *Hinode* (EIS, images of 195 Å intensities and Doppler shifts; Culhane et al. 2007); the *Hinode* Solar Optical Telescope (SOT, Ca II and *G*-band images; Tsuneta et al. 2008); the *STEREO*/SECCHI EUV Imager (EUVI, 171 Å and 195 Å images; Howard et al. 2008, Wuelser et al. 2004); the NRAO's Green Bank Solar Radio Burst Spectrometer (GBSRBS, metric radio spectrograms; White 2007); the Solar Radio Spectrograph (SRS, metric radio spectrograms) of the Air Force's Radio Solar Telescope Network (RSTN); *Wind* Waves (14 MHz–20 kHz spectrograms; Bougeret et al. 1995); and the Large Angle Spectroscopic Coronagraph (LASCO; Brueckner et al. 1995) on *SOHO*.

2.2. Event Overview

Figure 1 gives an overview of the 2006 December 6 event. The Sun was relatively clear of ARs at this time, with NOAA AR 10930 (spot area of ~500 millionths of a hemisphere) and NOAA 10929 (the small region to the northwest of 10930, spotless on December 6) being the only regions in the eastern hemisphere.

The Hα image in Figure 1, taken at 18:47 UT at the maximum of the soft X-ray flare, captures the Moreton wave (indicated by large white arrows) after it had propagated away from AR 10930. The wave, which was observed with certainty at 18:44 UT, is most prominent to the southwest of AR 10930. The image is scaled to enhance the visibility of the wave. The positions of filaments disrupted (at the given times) by the passage of the wave are indicated. A wave-induced oscillation of the large
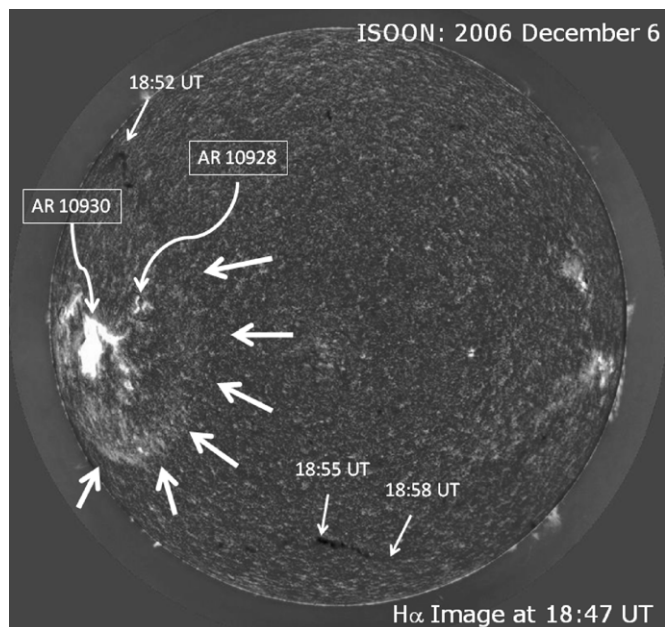
Figure 1. Overview of the solar eruption and Moreton wave of 2006 December 6. The Hα image has been scaled to emphasize the wave. The large arrows indicate the position of the wave at 18:47 UT. Smaller arrows indicate the positions of filaments that were disrupted by the wave at the given times as it propagated outward from the AR 10930.

(Animations (1a and 1b) of this figure are available in the online journal.)

filament near central meridian in the south has been discussed in detail by Gilbert et al. (2008). The 3B flare (located S06E63) is the dominant feature in AR 10930.

Figure 2 contains contours of the wave front as deduced from temporal running-difference (RD) images in the red wing of Hα from 18:43 UT until 18:51 UT. The contours are plotted on the red-wing RD image at 18:46 UT; the fourth contour corresponds to the displayed image. In heliographic coordinates, the contours from 18:43 to 18:51 UT yield angular spans from ∼240° to 280°. While the wave can be detected by inspection over this angular span, it is important to note that the amplitude of the disturbance was strongest in the south/southwest. This can be seen in the Hα centerline image in Figure 1 and in the series of red-wing minus blue-wing (Doppler) images in Figure 3, where the arrow drawn at 18:46 UT points in the general direction of the strongest part of the wave. The strength of the wave in four radial directions (south (270°), southwest (315°), west (0°), and northwest (45°)) is shown in Figure 4. The percentage changes are measured against a pre-flare base line image at 18:30 UT. The large amplitudes at distances $< \sim 5 \times 10^4$ km are due to the flare.

2.3. Origin of the Moreton Wave

2.3.1. Flare Gas Pressure Pulse Driver

2.3.1.1. Kinematics. The first three contours in Figure 2 (18:43–18:45 UT) were fitted with circles (dashed lines, ovals in projection) and the center of each of the three circles ("radiant point") was determined. These fits are plotted along with the contours on the Hα red-wing RD image at 18:45 UT in Figure 5. The radiant point (RP) for each contour is indicated by a color-coded plus sign. We obtained a composite RP ($X = -825 \pm 13$ arcsec, $Y = -92 \pm 6$ arcsec) by averaging the coordinates of the three RPs and using their scatter as an error estimate. It must be noted that the contour at 18:43 UT is of low
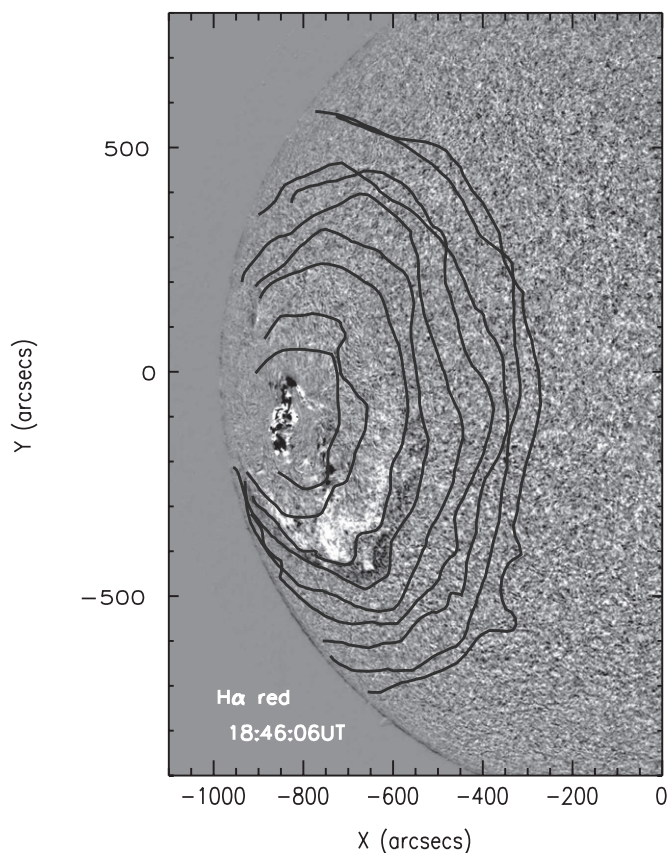

Figure 2. Position of the leading edge of the Moreton wave as determined in RD images in the red wing of Hα from 18:43 to 18:51 UT. The contours are drawn on the red-wing RD image at 18:46 UT. The origin of the *X, Y* coordinate system is at the Sun center.

confidence due to the poor contrast of the wave at that time, particularly to the north of the AR. Despite this difficulty, the RP determination is relatively robust, with the black rectangle in Figure 5 encompassing the three RPs in the figure as well as the two others determined from Doppler RD images at 18:44 UT and 18:45 UT.

A plot of the average deprojected distances of the wave leading edge contours (from red-wing RD images and Doppler RD images) from the composite RP versus time is given in Figure 6(a). The error bars indicate the deviation of the contours from the circular fits. The mean (linear fit, dashed line) velocity through the plotted points from 18:43 to 18:50 UT is ∼850 km s^{-1}. A constant deceleration fit extrapolated back to zero distance yields a nominal wave launch time of 18:41:13 UT. This fit has an initial velocity of ∼1125 km s^{-1} and a deceleration rate of 0.87 km s^{-2}.

Figure 6(b) contains time–intensity plots of *GOES* 1–8 Å soft X-rays and *RHESSI* 100–300 keV hard X-rays. The nominal wave launch time of 18:41:13 UT precedes the onset of 100–300 keV hard X-ray emission at ∼18:42 UT and the corresponding sharp increase (peak 1 minute derivative) in 1–8 Å emission between 18:42 and 18:43 UT (the interval indicated by dashed vertical lines). The Hα RD images in Figure 7 (scaled to enhance the frame-to-frame changes) show that a significant expansion of flare area occurred from 18:42 to 18:43 UT. Following the definition of Harvey (1971), this interval is the flare "explosive phase," the minute during which the integrated flare intensity first increases by >25% of the peak intensity (Figure 8(a)). Smith & Harvey (1971) showed that the
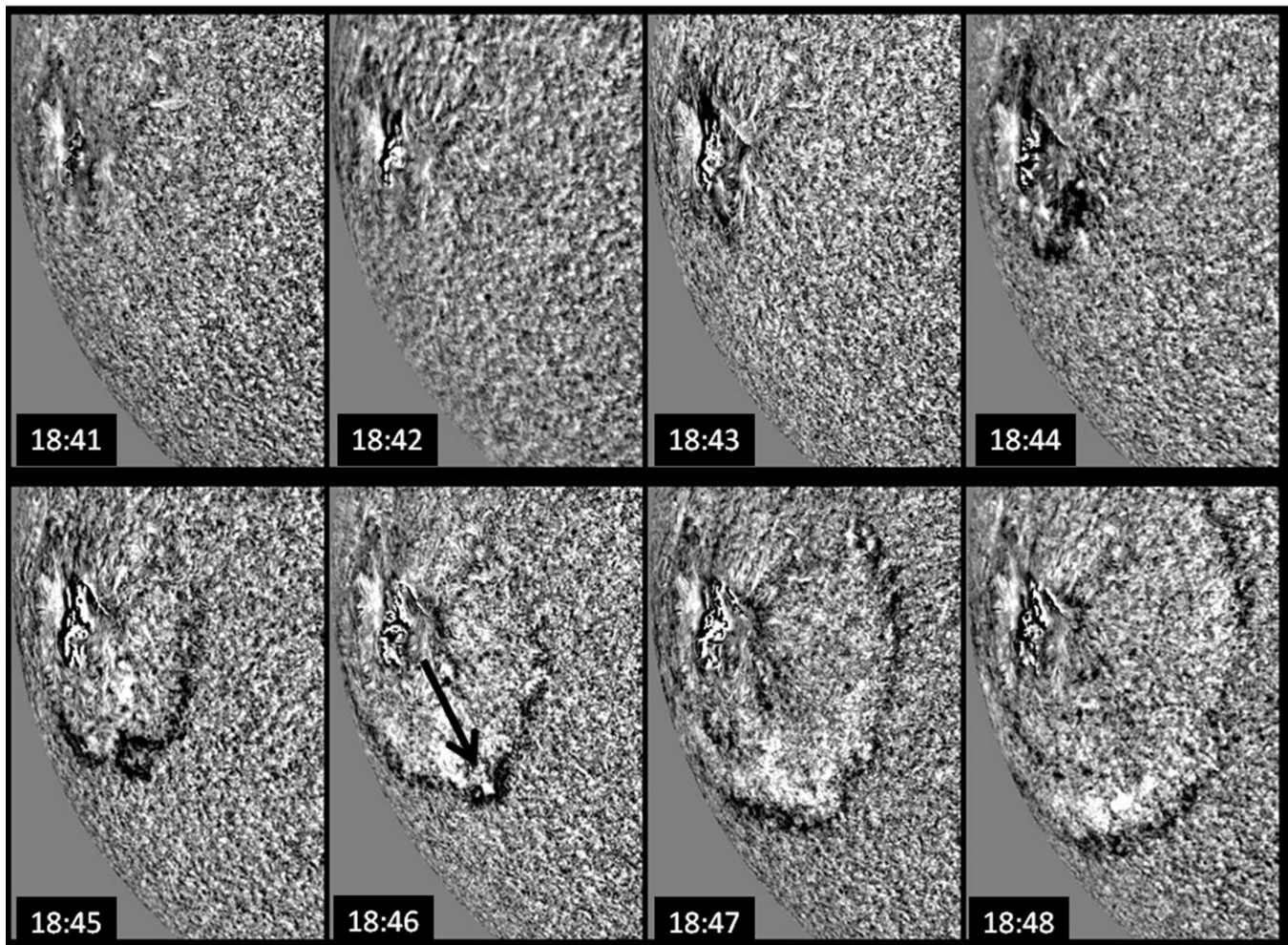
Figure 3. Doppler images (not running-differenced) from 18:41 to 18:48 UT. The arrow in the 18:46 UT frame points in the direction of the strongest wave amplitude.
(An animation of this figure is available in the online journal.)
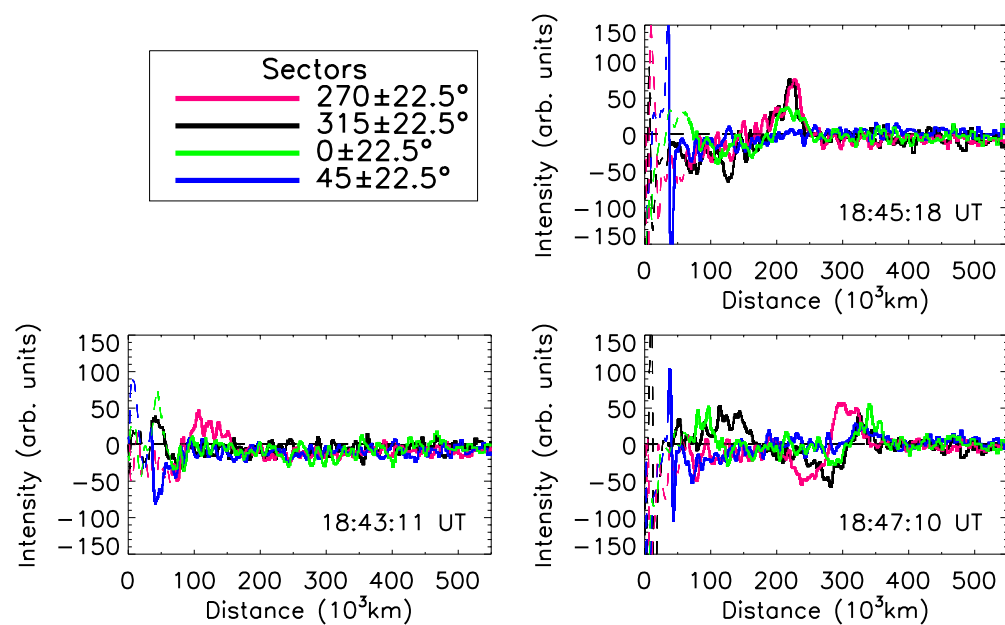

Figure 4. Amplitude of the perturbation derived from blue-wing minus red-wing images for various azimuthal sectors ($0° =$ west, $270° =$ south)) as a function of distance from the wave RP from 18:43 to 18:47 UT.
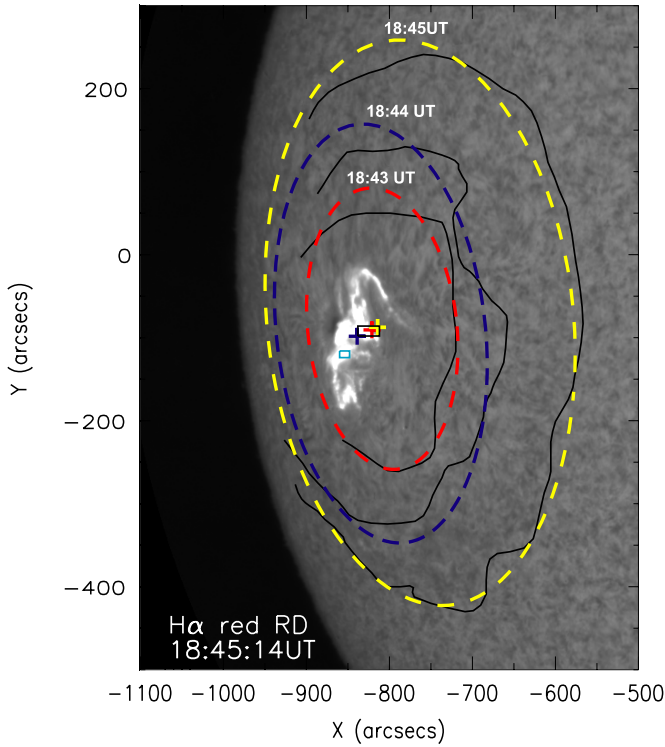
Figure 5. Position of the leading edge of the Moreton wave at 18:43 UT, 18:44 UT, and 18:45 UT (black lines, determined from RD images in the red wing of Hα) plotted on a RD centerline image at 18:45 UT, corresponding to the maximum of the Hα flare. The dashed-line circular fits (ovals in projection) are shown for each of the three contours and color-coded radiant points (plus signs) corresponding to each of the contours are shown. The black rectangle encompasses the positions of the radiant points (RPs) and the light-blue rectangle indicates the location of the centroid of the high-energy flare (FC).

(An animation of this figure is available in the online journal.)
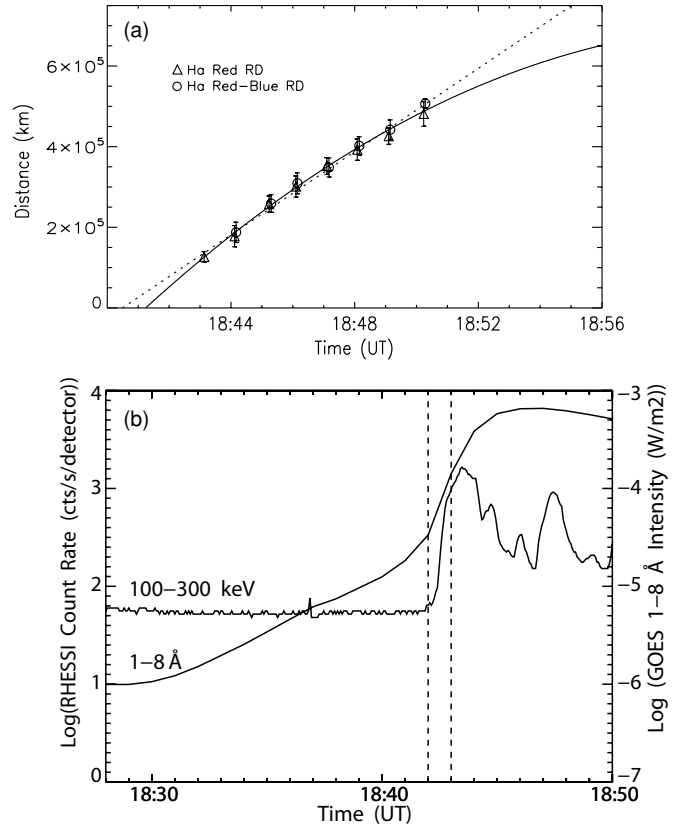

Figure 6. (a) Average deprojected distance of the leading edge of the wave (as measured in Hα red-wing and Doppler RD images) from the composite RP as a function of time. The dashed line fit indicates an average speed of ∼850 km s^{-1}. The quadratic fit is extrapolated to zero distance to indicate a lift-off time of 18:41:13 UT. (b) Time profiles of *GOES* 1–8 Å soft X-ray emission and *RHESSI* 100–300 keV hard X-ray emission. The explosive phase of the flare between 18:42 and 18:43 UT is indicated by dashed vertical lines.

onset of the explosive phase agrees well with the extrapolated origin of the Moreton wave. The high temporal resolution (3 s) 1–8 Å data in Figure 8(b) show that the impulsive heating in this event began no earlier than 18:42 UT. In our kinematic analysis below for the flare hypothesis, we will assume that the pressure pulse is initiated at 18:42 UT and allow 20 s for the acceleration of the driving disturbance (Vršnak & Cliver 2008). Both of these assumptions are favorable for the flare scenario because they maximize the time/distance that the initiating disturbance can propagate once the acceleration phase ends at 18:42:20 UT.

For the pressure pulse kinematics, we assume that the wave originates and begins decelerating at a constant rate at the end of the pressure pulse (t_O = 18:42:20 UT). The distance (d; at any time, t) to the wave is reckoned from the composite RP. The distance d_O (at time t_O) is the termination point of the assumed pressure pulse (d_O includes the pre-acceleration lateral extent of the flaring region). Let V_O be the velocity at t_O. For a simple constant deceleration case, the propagation distance is given as

$$d = d_O + V_O t + 0.5\, a t^2. \qquad (1)$$

Because we know the speed at 18:43 UT (∼1030 km s^{-1} from the constant deceleration fit in Figure 6(b)), assuming a value for V_O determines the average deceleration rate. Assigning V_O = 1400 km s^{-1} (the largest such value obtained by Warmuth et al. 2004a in their sample of 12 Moreton waves) implies a constant deceleration (a) of −9.2 km s^{-2} from 18:42:20 to 18:43 UT. This value for a is approximately four times the average deceleration determined by Warmuth et al. for the initial wave contours of

the events in their sample. For the first possible appearance of the wave at t = 18:43 UT, d = 1.2 × 10^5 (Figure 6(a)). Inserting the above values for the parameters in Equation (1) and solving for d_O yields a value 7.1 × 10^4 km. Because of the uncertainty regarding the first appearance of the wave, we calculated d_O for the 18:44 UT contour, using d = 1.8 × 10^5 km and t = 100 s. In this case, a has a more reasonable value of −4.2 km s^{-2} and we obtain d_O = 6.1 × 10^4 km. Both of these d_O values exceed the order-of-magnitude upper limit for the pressure pulse scale length of ∼10^4 km (Vršnak & Cliver 2008). Moreover, it places the end point of the pressure pulse acceleration *beyond the borders of the AR* to the northwest of the RP. For a pressure pulse of 20 s duration, beginning at 18:42 UT, to excite a wave at 1.8 × 10^5 km at 18:44 UT would require the following, relatively extreme (Warmuth et al. 2004a; Vršnak & Cliver 2008), parameters—pressure pulse acceleration of 100 km s^{-2}; V_O of 2000 km s^{-1}; and a constant deceleration rate of −10.2 km s^{-2}—with d_O = 3.1 × 10^4 km. The velocity time profile for such a driver and its wave are shown by the red line in Figure 9, with the transition from the dashed line to the solid line marking the end of the pressure pulse and the onset of the wave. The very strong deceleration that the wave must undergo after 18:42:20 in order to match the observed wave speed at 18:44 UT, despite generous assumptions on the timing/duration of the pressure pulse, argues against a pressure pulse driver for the Moreton wave of 2006 December 6. That said, it must be kept in mind that the order-of-magnitude upper limits used for the range of the gas pressure pulse (∼10^4 km)
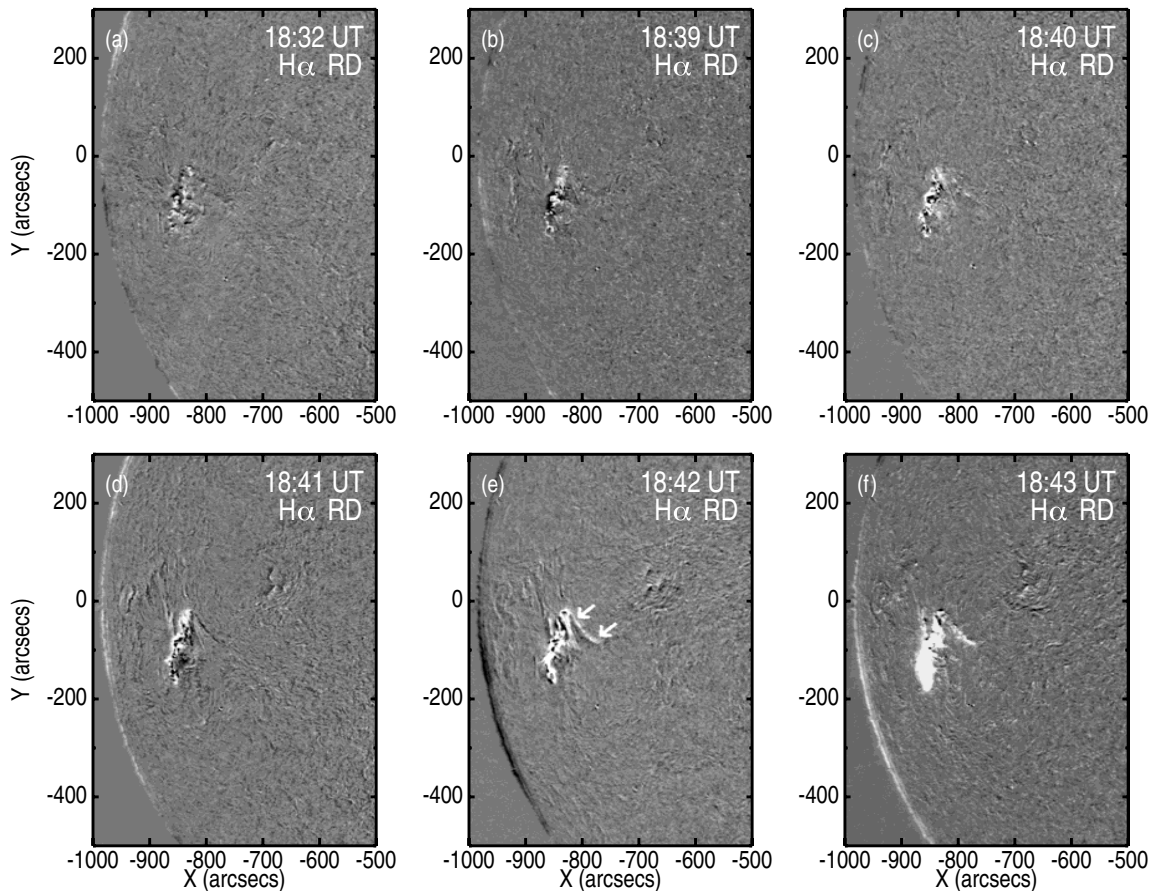
Figure 7. (a)–(f) Series of Hα RD images scaled to enhance flare brightening showing the development of the 3B flare from onset at 18:32 to its explosive phase from 18:42 to 18:43 UT. Frame (e) shows the extension of the flare to the northwest (white arrows) at 18:42 UT and frame (f) shows the sudden expansion of flare area and brightness in the principal part of the flare at 18:43 UT that characterizes the explosive phase.

and the peak acceleration rate ($\sim$100 km s^{-2}) are not observed quantities, but estimates.

2.3.1.2. Spatial Relation of the Radiant Point and the Flare Center. If a gas pressure pulse (flare blast) was the source of the wave on 2006 December 6 we might expect the centroids of energetic flare emissions, magnetic energy conversion, or impulsive flare dynamics to be located close to the RP of the wave. We compare the spatial relationship of the composite RP to these various signatures in Figure 5. The light-blue rectangle centered at ($-854''$,$-120''$) in this figure encompasses the centroids of the following flare signatures: (1) *RHESSI* X-ray emission (mean position of ($-853''$,$-122''$) based on 6–12 keV ($-855''$, $-117''$) and 100–300 keV ($-850''$, $-126''$)); (2) WL emission (mean position of ($-856''$, $-116''$) based on the brightest ISOON WL emission ($-854''$, $-118''$; single observation at 18:45 UT) and *Hinode G*-band emission ($-858''$, $-114''$; 18:43.6 UT))[13]; (3) magnetic force change (mean position of ($-847''$, $-122''$) based on downward ($-841''$, $-129''$; 9.1 $\times$ 10^{21} dyn) and upward ($-853''$, $-116''$; 1.4 $\times$ 10^{21} dyn)) force changes inferred from GONG magnetic field measurements between 18:40 and 18:44 UT)[14]; and (4) origin

of an ejection (spray emanating from ($-860''$,$-120''$) with a projected speed of $\sim$550 km s^{-1} observed by *TRACE* at 1600 Å (see animation 1a associated with Figure 1 in the online version) from $\sim$18:42:30 to 18:43 UT). While the positions of the wave RP (black rectangle) and "flare center" (light-blue rectangle) in Figure 5 do not overlap, the significance of the separation is less than 2σ (5.0 ($\pm$2.7) $\times$ 10^4 km). As a result this test does not provide a strong argument either for or against the flare driver.

2.3.2. CME Driver

2.3.2.1. Evidence for a CME. Following an extended data gap that began on December 4, the LASCO coronagraph resumed taking images at 20:12 UT on December 6.[15] An RD image at 20:24 UT shows CME remnants, principally in the southeast, of a halo CME. Indirect evidence for a CME is provided by the associated intense (X6.5) soft X-ray event, an interplanetary (IP; 16 MHz–30 kHz) type II burst beginning at 19:00 UT (http://lep694.gsfc.nasa.gov/waves/waves.html),[16] and an enhancement of >100 MeV protons observed by *GOES* late on December 6. Yashiro et al. (2005) reported that all flares >X3 during 1996–2004 were associated with CMEs and it is generally accepted, following Cane et al. (1987), that all IP

---

[13] Following the work of Hudson et al. (1992) using *Yohkoh* SXT, Isobe et al. (2007) and Wang (2009) have used photospheric *G*-band emission observed by *Hinode* as a proxy for WL emission.

[14] The total unsigned force change from 18:30 to 18:44 UT ($\sim$2 $\times$ 1022 dyn) was the largest yet inferred during a solar flare from GONG field change measurements (Petrie & Sudol 2010). The centroid of the 18:30–18:40 UT force changes (-842, -109) was located somewhat closer to the radiant point than to the flare center.

[15] A corresponding EIT data gap lasted until late on December 7.

[16] Curiously, given the close implied/observed association between Moreton waves and type II bursts (Uchida 1974a, 1974b; Smith & Harvey 1971; Harvey et al. 1974; Warmuth et al. 2004a), the Sagamore Hill (RSTN SRS) 180–25 MHz and Green Bank (GBSRBS) 70–10 MHz (sweep-frequency) spectra show no evidence for a type II burst, although we cannot rule out the presence of such a burst under bright flare continuum observed from $\sim$18:44 to 19:02 UT.
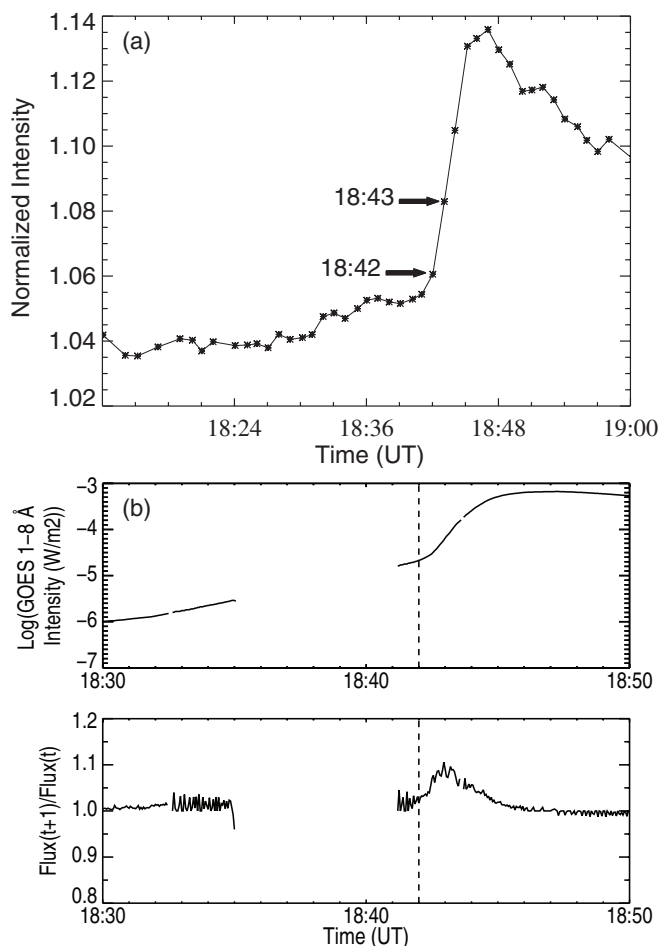
Figure 8. (a) Normalized Hα intensity of the 3B flare on 2006 December 6 as a function of time. The arrows indicate the explosive phase of the flare from 18:42 to 18:43 UT. (b) Top panel: high-time resolution (3 s) time profile of the 1–8 Å flare observed by *GOES*. Bottom panel: the derivative of the intensity. The dashed vertical line indicates the earliest possible onset of the flare impulsive/explosive phase. The noise in the derivative on either side of the data gap appears to be an artifact related to a variable averaging period (multiples of 3 s) for these times.

Figure 9. Time profiles of the modeled lateral velocities of the flare pressure pulse and wave (red solid/dashed line) and CME lateral expansion and wave (black solid/dashed line).

(A color version of this figure is available in the online journal.)

type II bursts are driven by CMEs. Finally, large solar energetic particle (SEP) events are thought to result from CME-driven shock waves (e.g., Kahler et al. 1984; Cliver et al. 2004a).

2.3.2.2. Kinematics. What constraints do the observations place on the CME hypothesis? The first definite appearance of the Moreton wave at 18:44 UT is nominally consistent with a CME driver, because the wave onset falls within the time period from 18:42 to 18:47 UT bounded by the onset of the fast rise phase (first 1 minute flux derivative ⩾2; Cliver et al. 2004b) and the maximum of the soft X-ray burst (Figure 6(b)). This interval generally, though not always (Maričić et al. 2007), corresponds to the rapid acceleration phase of the CME in eruptive flares (Zhang et al. 2001; see also Temmer et al. 2008 for a complementary analysis based on hard X-ray bursts).

For the 2006 December event, we are able to bring a new kind of evidence to bear on the main acceleration phase of the CME. Following Sudol & Harvey (2005), Petrie & Sudol (2010) used 1 minute GONG magnetograms to characterize changes in the photospheric longitudinal magnetic field for a sample of ∼80 M- and X-class flares from 2001 to 2007. This sample included the 2006 December 6 flare that exhibited one of the largest field changes (∼445 G) they observed. The time
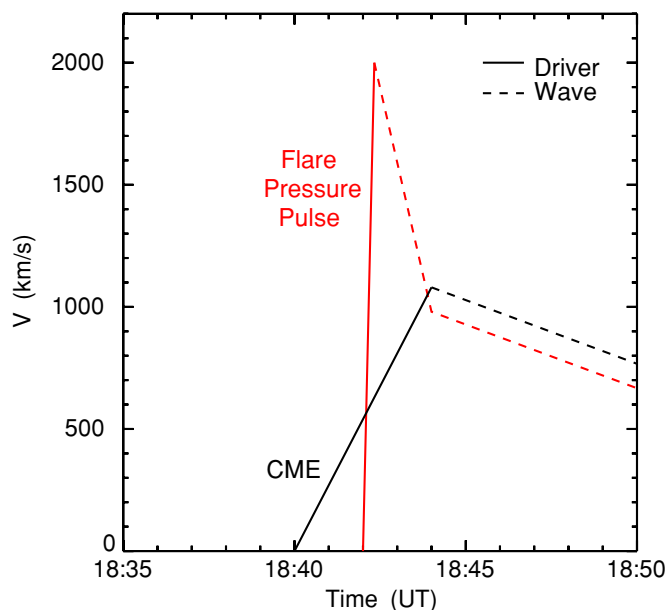
variation of the Lorentz force applied to the photosphere in this event (obtained via a calculation first given in Anwar et al. 1993, and subsequently used by Hudson et al. 2008), is given in Figure 10. Since these force changes (amounting to ∼2 × 10^{22} dyn) result from a change in the coronal magnetic fields, we assume that they are a reflection of the cataclysmic arrangement of fields manifested by the CME launch. *Specifically, we make the assumption that the peak in the net force time profile from 18:40 to 18:44 UT corresponds to the main acceleration phase of the CME.*

To investigate the possibility that the CME drove the Moreton wave in this event, we assume that the CME accelerated laterally at an average rate of 4.5 km s^{-2} from 18:40 to 18:44 UT (after which the CME begins its coasting or slow deceleration phase). This is a strong acceleration but comparable to the average vertical rate of ∼4.5 km s^{-2} reported by Zhang & Dere (2006) for the X9.4 event on 1997 November 6.[17] This rate is also comparable to the 4.8 km s^{-2} rate (maintained for 2.7 minutes) assumed by Temmer et al. (2009) to model the Moreton wave associated with an X3.8 flare on 2005 January 17. Substituting into Equation (1) then yields $d \sim 1.3 \times 10^5$ km. Most of the remaining distance to the leading edge of the wave to the northwest at 18:44 UT (∼1.8 × 10^5 km) is accounted for by the ∼3.5 × 10^4 km distance between the RP and the border of the AR in this direction, assuming that the region erupts to form the CME. One possibility for the remaining ∼1.5 × 10^4 km might be lateral expansion of the CME source (arcade swelling) during the CME initiation phase, in association with the rise in soft X-ray emission (Figure 6(b)) from ∼18:30 to 18:40 UT[18] and the accompanying change in the magnetic field (Figure 10). Zhang et al. (2001) found that such X-ray precursors were accompanied by a slow ascension (<80 km s^{-1}) of CMEs. For the above assumptions, the CME horizontal speed at 18:44 UT

---

[17] Lateral expansion at a rate ∼5 km s^{-2} during 2.3 minutes was observed for the 1997 November 6 event (see Figure 14 in Cliver et al. 2004b).
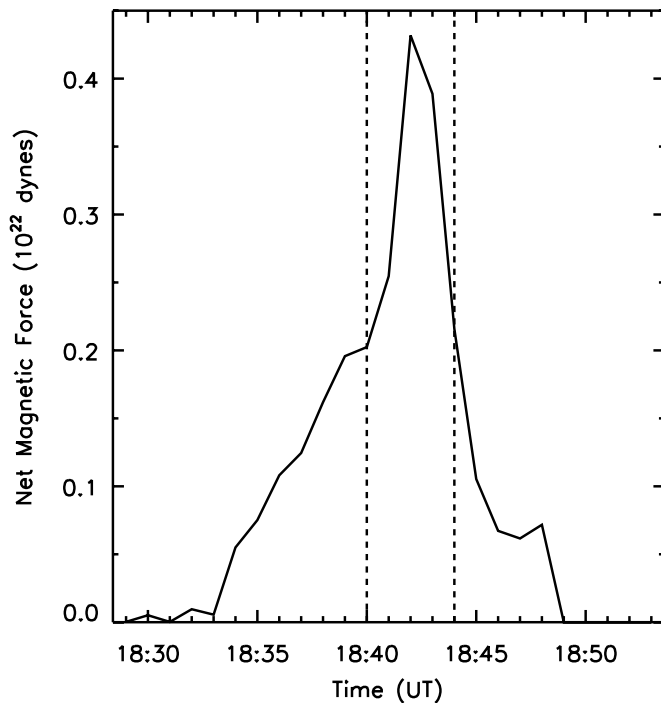[18] Earlier increases on an overall rising profile began at ∼17:45 UT and 18:05 UT.

Figure 10. Time variation of the net downward Lorentz force on the photosphere during the 2006 December 6 3B/X6.5 flare as calculated from the longitudinal field change recorded by the GONG magnetograph at Cerro Tololo. We assume that the coronal field changes responsible for the impulsive peak in the force from 18:40 to 18:44 UT indicate the cataclysmic field changes associated with the main acceleration phase of the CME.

is 1080 km s^{-1}, somewhat above the $\sim$980 km s^{-1} at this time obtained from the constant deceleration fit for the Moreton wave (Figure 6(a)). A plot of the velocity profile of the CME driver and the associated wave (black line, solid and dashed, respectively)

is given in Figure 9 for comparison with that of the pressure pulse driver. An alternate possibility is that the CME accelerates at 5.5 km s^{-2} for 3 minutes (from 18:40 to 18:43 UT) and then the wave decelerates at the observed rate of -0.87 km s^{-2} thereafter. This provides a better velocity fit at 18:44 UT than for the CME case depicted in Figure 9 and removes the need to invoke pre-eruption swelling of the arcade. Or we could extend the higher rate of lateral CME acceleration through 18:44 UT to account for the fact that the leading edge of the shock wave in the corona leads the chromospheric "hem of the sweeping skirt" (e.g., Vršnak et al. 2002; Warmuth 2007). We note that the 5.5 km s^{-2} acceleration rate will also accommodate the earlier wave onset at 18:43 UT. Since we lack CME observations in the low corona, the velocity profile in Figure 9 is illustrative rather than compelling. Nonetheless, the assumptions for driver timing and the acceleration rate seem reasonable and the resultant velocity profile appears more natural than is the case for the gas pressure pulse.

2.3.2.3. Spatial Relationship of the Wave to the Flare and CME Source. An Hα image of AR 10930 made at 18:30 UT, taken shortly before the reported flare onset, and the closest available MDI magnetogram (17:39 UT) are given in Figures 11(a) and (b), respectively. In this figure, we have indicated (with a white dashed oval) an "arm" of negative polarity with its "shoulder" rooted to the northern portion of the principal part of AR 10930 and extending to the southwest before turning further toward the south at the "elbow." We highlight this feature because it marks the approximate north and westward boundary of an arcade of loops (seen in *TRACE* 195 Å images). We postulate that this arcade erupted to drive the wave via a coronal shock. The arcade has its eastern boundary in the positive polarity fields in the main part of the region. F$_1$ and F$_2$ denote two narrow filaments, tracing the magnetic neutral line in AR 10930, that are connected at the shoulder of the arm. F$_1$ threads the strong complex field to
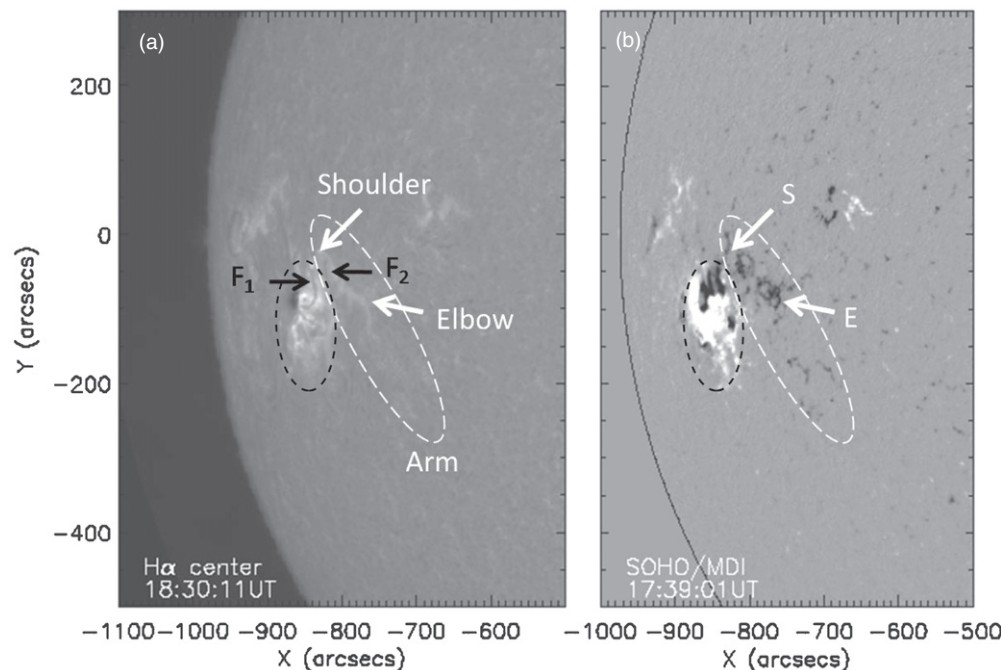

Figure 11. (a) Hα image of AR 10930 at 18:30 UT. An "arm" of faint plage emission corresponding to a ridge of negative polarity in the western part of the AR is outlined with a white dashed oval. The "shoulder" (S) and "elbow" (E) of the arm of negative polarity are marked by arrows as are two narrow filaments (F$_1$ and F$_2$). The black dashed oval outlines the principal part of the AR and the location of the main flare. (b) The MDI magnetogram at 17:39 UT.
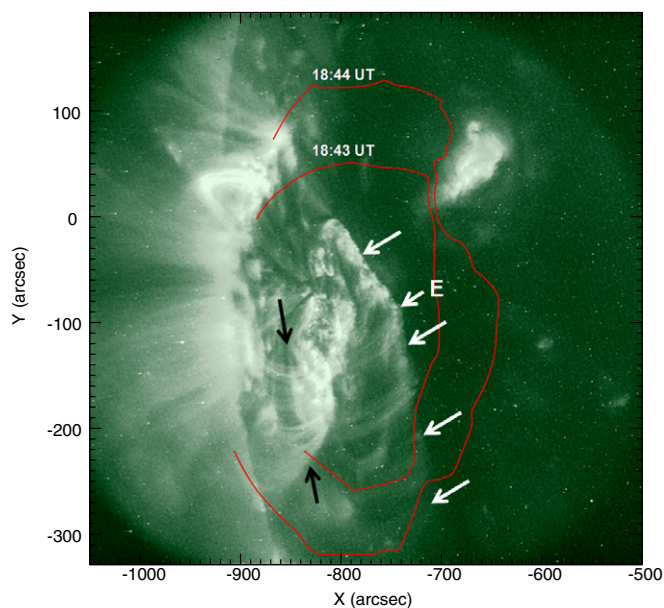
Figure 12. *TRACE* image at 08:01 UT showing the western arcade that we link to the Moreton wave (white arrows) and the eastern arcade associated with the main flare (black arrows). The elbow (E) of the negative polarity "arm" is indicated. The wave contours (thin red lines) at 18:43 UT and 18:44 UT are adjusted to take solar rotation into account. The *X*-coordinates have been shifted to correspond to the time of the waves.

Figure 13. A 10830 Å image of AR 10930 at 18:59 UT showing dark flare ribbons marking the footprint of the western arcade in the south (traced by white dotted line) and the wave leading edge at 18:43 and 18:44 UT (solid red lines). The arrow points in the direction in which the wave was initially strongest in centerline Hα images.

the east of the arm (black dashed oval) corresponding to the site of the principal flare in this event. F_2 separates the northern part of the arm from the main part of the AR. F_1 and F_2 are separated by a region of positive polarity and are mentioned here as tracers of the large-scale chromospheric neutral line. The ejection observed at 1600 Å by *TRACE* indicates the eruption of F_1 (see animation 1a associated with Figure 1 in the online version) but F_2 remains intact during the flare impulsive phase and is apparent in Hα images at ∼19:00 UT.

The arcade of loops to the west of AR 10930 is indicated by white arrows in the *TRACE* 195 Å background image 08:01 UT (Figure 12). The arcade associated with the main flaring region to the east of the AR is marked by black arrows. A *TRACE* 195 Å data gap extends from 09:48 UT on December 6 until 01:18 UT on December 12. We assume that the loops shown at 08:01 UT do not change substantially prior to the X6.5 flare (early EUVI images show that this assumption holds until at least ∼17:00 UT). The thin red lines trace the leading edge of the wave at 18:43 UT and 18:44 UT.

The ISOON He I 10830 Å image at 18:59 UT in Figure 13 allows us to identify the footprint of the western 195 Å arcade. It takes into account any possible evolution of the arcade between 08:01 UT and the X6.5 flare. In Figure 13, the white-dotted line traces the dark 10830 Å flare ribbons (see Harvey & Recely 1984) for the southern part of the arcade. The wave contours at 18:43 UT 18:44 UT are also drawn in the figure. The He I flare ribbons show reasonable agreement with the wave contour in the south at 18:44 UT, corresponding to the first unambiguous appearance of the wave in centerline Hα. The white arrow in Figure 13 points in the direction of maximum wave amplitude (see Figures 3 and 4).

The Hα flare began at 18:32 UT and evolved as a series of bright points until 18:41 UT in the strong complex field in the east of the region (Figures 7(a)–(d); all images scaled to enhance wave visibility). At 18:42 UT, a more widespread brightening in the eastern part of the AR was accompanied by flaring in the
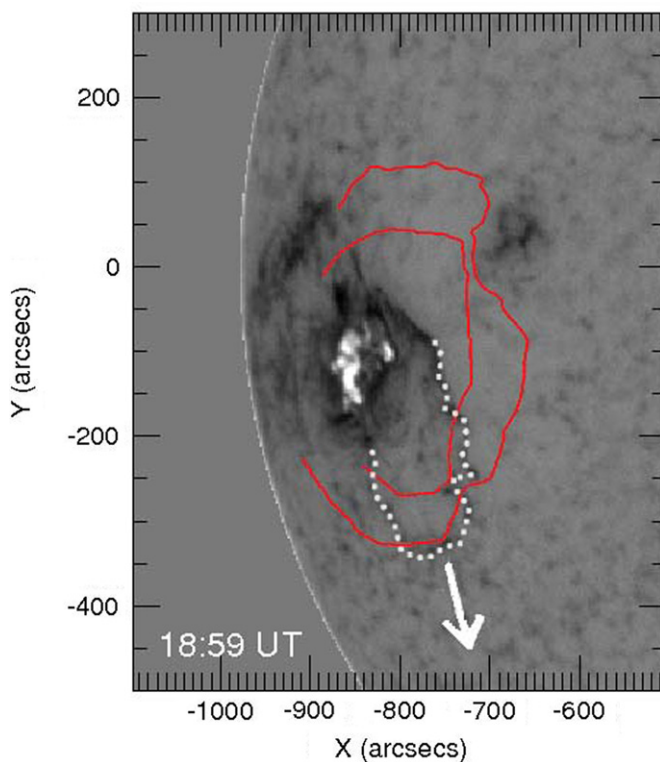
arm above the elbow (indicated by white arrows; Figure 7(e)). From 18:42 to 18:43 UT (Figures 7(e)–(f)), there is a dramatic increase in flare area and brightness in the strong magnetic fields in the east (black dashed oval in Figure 11).

The Hα centerline RD images in panels (a)–(c) in Figure 14 shows the advance of the leading edge of the Moreton wave from 18:43 to 18:45 UT as determined from these images (thick red lines). Panels (d)–(f) show the corresponding red-wing RD images and wave contours (thin red lines). Both of these sets of images are scaled to enhance the visibility of the wave. The He I 10830 Å ribbons, tracing the footprint of the 195 Å arcade, are shown by a dotted black line in frames (a)–(f). At 18:43 UT (Figure 14(a)), the wave was not observed in the Hα centerline image. As can be seen in the Doppler image at 18:43 UT in Figure 3, the wave, or "propagating disturbance" as we prefer to call it at this stage of its development, lacks a well-defined leading edge outside of the confines of the AR, although features within the AR appear in sharp relief. Thus in Figure 14(d), the leading edge of the disturbance in the south cuts across the arcade of loops. The wave makes its first appearance in a Hα centerline image at 18:44 UT (Figure 14(b)), as a short arc near the northeast edge of the arcade. Also in this image we begin to see an extension of the flare ribbon south of the elbow. In Figure 14(e), the leading edge of the red-wing wave at 18:44 UT is roughly aligned with the footprint of the 195 Å arcade in the south. Note that the principal darkening in this image remains inside the confines of the AR. To the north and west the wave extends beyond AR 10930 while avoiding AR 10929 by passing through either side of it (the "indent" in the contour). At 18:45 UT (Figure 14(c)), the western "arm" brightens from
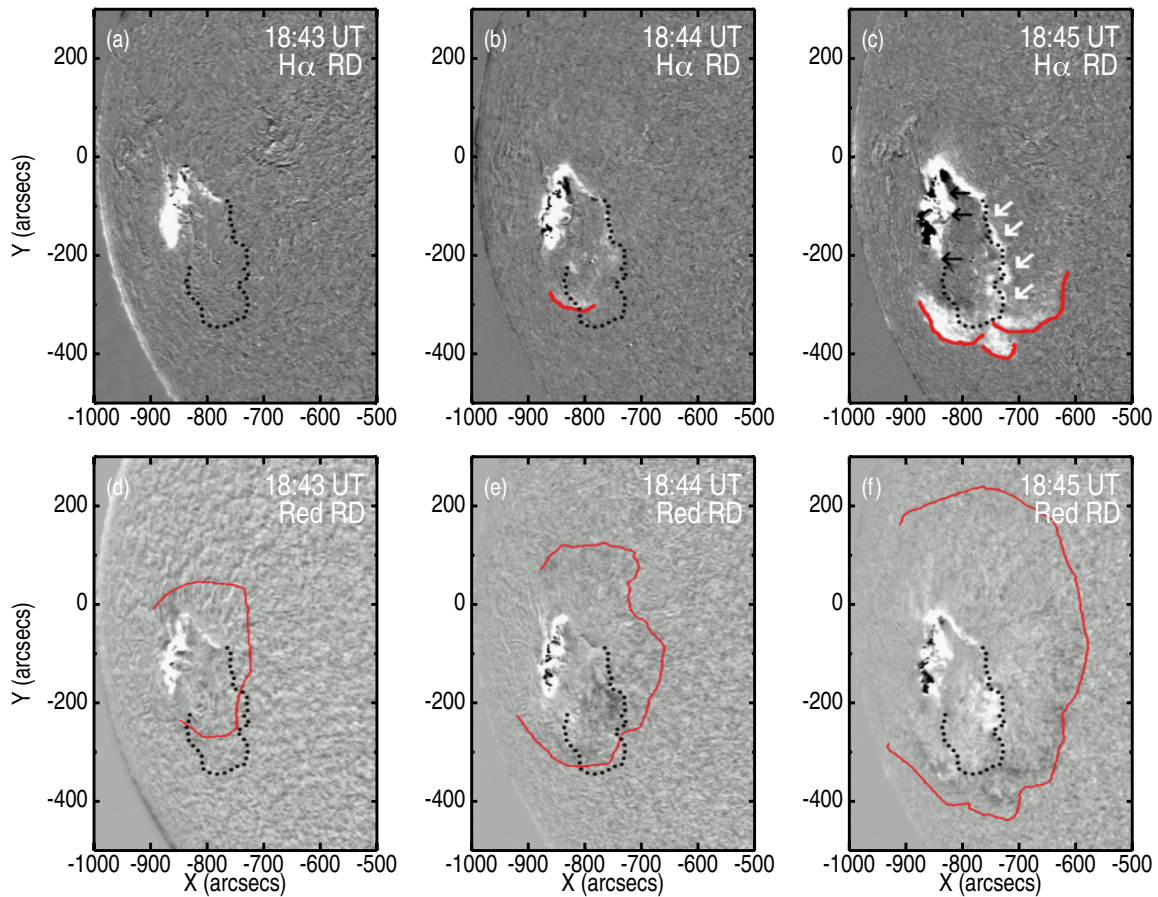
Figure 14. (a)–(c) Running-differenced Hα centerline images at 18:43 UT, 18:44 UT, and 18:45 UT, respectively. The thick solid red lines show the wave leading edge as determined in these images. The dotted black line shows the footprint of the western arcade as delineated in the He I 10830 Å line. In (c), the white (black) arrows point to negative (positive) polarity magnetic fields. (d)–(f) Same as (a)–(c) but for RD red-wing images and wave contours. In these frames, the leading edge of the wave is traced by a thin solid red line. For both series (centerline and red-wing), the images have been scaled to increase the visibility of the wave.

the shoulder southward along the negative polarity ridge (white arrows). This brightening is accompanied by an increase in area in the western part of the main flare in regions of positive polarity (black arrows). In images that are not "overexposed," the flare brightening above the elbow at 18:45 UT occurs slightly north of the ribbon that first appeared at 18:42 UT, suggesting the expansion of flare ribbons as higher loops reconnect. In Figure 14(c), we see that the arc of the wave near the southeast tip of the arcade at 18:44 UT has strengthened and is now accompanied by a similar arc off the western flank of the arcade. These arcs appear to be pivoting about a point at the tip of the arcade. We speculate that the smaller arc between them to the south results from their overlap and reinforcement.

The various brightenings from 18:32 to 18:45 UT (Figures 7 and 14) indicate a three-ribbon flare (or, equivalently, two adjacent two-ribbon flares with a shared ribbon). The main flare is located in the eastern part of AR 10930 (strong field region; dashed black oval in Figure 11). The secondary flare links the positive polarity ribbon of the main flare (black arrows in Figure 14(c)) with the negative polarity arm (white arrows) west of the region. This picture is independently substantiated by a series of Ca II (H-line) filtergrams from *Hinode* SOT (not shown here).

To reiterate, the eruption traced by the western two-ribbon flare began in the northern part of AR 10930. At 18:43 UT only the part of the arm above the elbow was involved (Figure 7(b)).

The extension of flare brightening below the elbow occurred from 18:44 to 18:45 UT (Figures 14(b) and (c)). The evolution of the Moreton wave mimics the north-to-south development of the eruption. The first appearance of a distinct wave front detached from the AR occurs in the northwest at 18:44 UT (Figures 3 and 14(e)). A discrete, separated leading edge is not apparent in the south until 18:45 UT (Figures 3 and 14(c) and (f)).

An mpeg animation showing the development of the eruptive flare and the Moreton wave from 18:30 to 18:50 UT is available in the online version (see animation 1b associated with Figure 1). This animation shows the merging and coalescence of the two arcs on the flanks of the western arcade at 18:45 UT into the single well-defined wave front seen in Figure 1 at 18:47 UT.

We believe that the various observations summarized in animation 1b are best understood if the contour at 18:43 UT in Figures 2, 5, and 12–14 is viewed as a tracer of the wave (or its progenitor) in the north and west, and of the arcade eruption in the south. The contours at 18:43 UT and 18:44 UT drawn on the 195 Å image in Figure 12 and on the He I 10830 Å image in Figure 13 suggest that the eruption is proceeding southward along the western arcade. We suggest that the arcade expands laterally as it erupts, driving a wave off its flanks. Such eruption is supported by the Hα brightening along the western arm (and on the shared ribbon of the main flare) at 18:44–18:45 UT. This delayed phase of Hα brightening is accompanied by a secondary peak in >100 keV emission (Figure 6(b)).
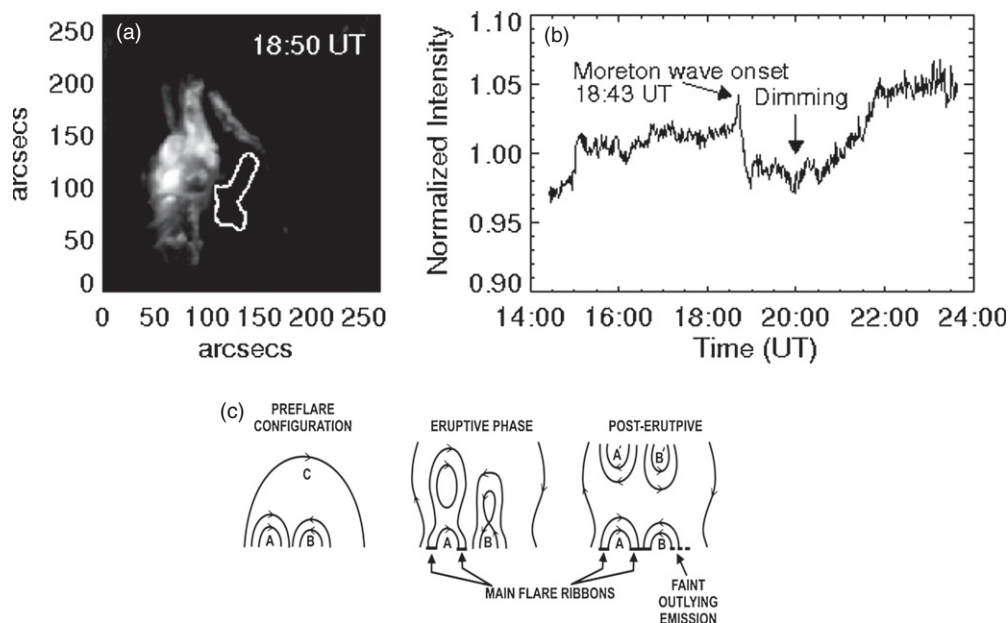
Figure 15. (a) Hα centerline image at 18:50 UT with the Hα darkening region traced in white. (b) The time intensity plot shows the Hα darkening in this region following the eruptive flare. (c) A cartoon taken from Neidig et al. (1997) to illustrate the cause of the darkening—absorption by faint out-lying unresolved post-eruption loops in a weak field region adjacent to the main flare. Note that the magnetic polarities in this figure do not match those for the 2006 December 6 event. They could be easily modified to do so but we show the figure of Neidig et al. (1997) unaltered because of its remarkable resemblance to the 2006 event.

2.3.2.4. Hα Darkening in the Western Arcade. In Figures 15(a) and (b), we show that a portion of AR 10930 between the ribbons of the western flare underwent an unusual darkening in Hα following the eruption.[19] Neidig et al. (1997) have previously reported such dimming in 'magnetically neutral' regions lying outside but adjacent to bright flare emission. Their description of these darkening regions as being "bordered by ridges of oppositely-poled field, where one border is shared in common with a flare ribbon," applies to the region indicated in Figure 15(a) in the western arcade in the 2006 December 6 event. Neidig et al. found that, "Simple models for post-flare loops incorporating the results of statistical equilibrium calculations readily demonstrate that darkenings of several percent (consistent with our photometric measurements) can be produced by loop structures of cross-sectional diameter $\approx 10^2$ km (unresolved by patrol instruments) and containing gas at densities 5×10^{10}–5×10^{11} cm^{-3} and temperatures 8000–15000 K." The EIS Intensity and Doppler images from *Hinode* for the 2006 December 6 event are given in Figures 16(a) and (b), respectively, where it can be seen that a system of faint loops do indeed overlie the western arcade (see Figure 12 for a view of the pre-eruption loops). In Figure 16, we have traced (white contour) the Hα dimming region from Figure 15(a). The redshifted material along and at the footpoints of the overarching fieldlines is a characteristic feature of post-eruption loops as is the blueshifted material lying beyond the footpoints that represents outflow from erupted loops that have yet to reconnect (Czaykowska et al. 1999). One version of the cartoon Neidig et al. (1997) used to explain the Hα darkening they observed (reproduced here as Figure 15(c)) could be applied with little modification to the 2006 December 6 event.

2.3.2.5. A Role for the Eastern Arcade in Generating the Moreton Wave? Here we consider the possibility that the
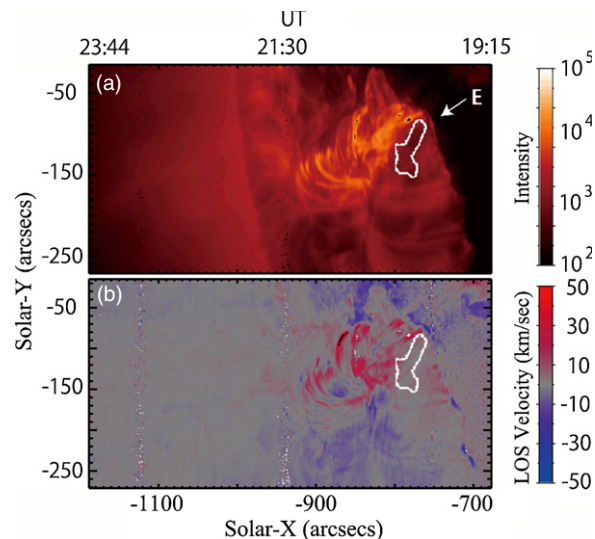
---

[19] We tested three other regions on the periphery of 10930 and in each case found no extended dimming below the pre-event level as observed in Figure 16(b).

Figure 16. *Hinode* EIS scan images of AR 10930 showing (a) log intensity at 195 Å; and (b) Doppler velocity (km s^{-1}). The times at the top of the figure give the start, mid-point, and end of the scan period. The white contours mark the position of the Hα dimming region in Figure 15(a).

Moreton wave was driven not by the eruption of the western arcade but by the lobe of the CME (Figure 15(c)) that originated in the strong complex fields associated with the main flare in the east of AR 10930. Could expansion of this lobe of the CME have "overpowered" the part of the eruption associated with the western arcade and driven the strong wave to the southwest? This supposition, consistent with the "big flare/CME syndrome" (Kahler 1982), is contradicted by the eastward movement (toward the arcade of the main flare) of the eastern flank of the Moreton wave (or its progenitor) from 18:43 to 18:45 UT (Figures 14 and 16). There is, however, another way that eruption of the main arcade may have contributed to the wave. The strong blueshifted region near the "shoulder" in Figure 16(b), which originates in a weak negative polarity

region (Figure 11(b) suggests a transient coronal hole; Harra et al. 2007; Imada et al. 2007), plausibly the footpoint of a flux rope threading the main part of the AR. Muhr et al. (2010) recently reported a Moreton wave event in which it appeared that two separate wave ignition centers corresponded to footpoints of a coronal flux rope. For the 2006 December 6 event then, flux rope eruption of the eastern arcade could account for the northern part of the Moreton wave and may also have triggered the eruption of the western arcade to which we attribute the wave in the southwest.

3. CONCLUSION

3.1. Summary and Interpretation

The Moreton wave on 2006 December 6 spanned $\sim 270°$ in azimuth and was observed directly for ~ 10 minutes as it propagated at a speed of ~ 850 km s^{-1} across the solar disk, reaching distances of $\sim 5 \times 10^5$ km from the parent AR. While the wave itself was well observed, investigation of the wave driver was hampered by the virtual absence of CME and coronal images. Nonetheless, kinematic analysis of this event favors a picture in which the wave is driven by the eruption of a CME rather than by a sudden expansion of flare volume due to explosive heating. The flare scenario requires a strong early wave deceleration to match the observed wave speed. We infer a CME acceleration rate consistent with that of other large events by assuming that an interval of strong impulsive magnetic field change observed near the rapid rise of the flare (Petrie & Sudol 2010) corresponds to the main acceleration phase of the CME. The following lines of evidence link a magnetic arcade overlying a region of weak field on the western periphery of AR 10930 and the Moreton wave: (1) the north-to-south evolution of both the eruption in the western arcade and the wave (Figure 14); (2) the conformity of the disturbance contour at 18:44 UT with the southern tip of the 195 Å arcade (Figure 12); (3) the alignment of the He I 10830 flare ribbons (and the overlying arcade) with the southwest direction of the wave (Figures 3, 4, 13, 14(c) and (f)); and (4) the coalescence of two separate wave fronts, each identified with a flank of the arcade, to form a contiguous Moreton wave (Figures 1, 14(c) and (f)); see also animation 1a in the online version). Hα foot point brightenings, blue shifts at the foot points of the 195 Å arcade, He I 10830 Å flare ribbons, and a darkening of the chromosphere under the arcade (attributed to absorption by post-eruption Hα loops; Neidig et al. 1997) indicate that the western arcade erupted to drive the wave. The two-ribbon Hα flare resulting from this eruption had one ribbon in common with the main part of the flare in the eastern part of the AR.

The simplest interpretation of the data for this event is that the magnetic arcade to the west and south of the main flaring region erupted to form a CME that drove the shock responsible for the Moreton wave as it expanded laterally. Dere et al. (1997) and Zhang et al. (2001) presented early evidence for lateral expansion of CMEs in the low corona. The cartoon in Figure 17 shows the eruptive flare model (e.g., Figure 3 in Forbes 2000), with a Moreton wave added. Once the lateral expansion of the CME stops, both the coronal shock and the associated Moreton wave propagate freely. As seen in Figures 3, 4, and 6(a), the deceleration, broadening, and damping characteristic of freely propagating waves (Warmuth et al. 2004b) were all observed.[20]

Our speculation equating the interval of strong field changes with the main phase of CME acceleration (Section 2.3.2.2;

---

[20] The propagation characteristics of the 2006 December 6 event will be presented elsewhere.
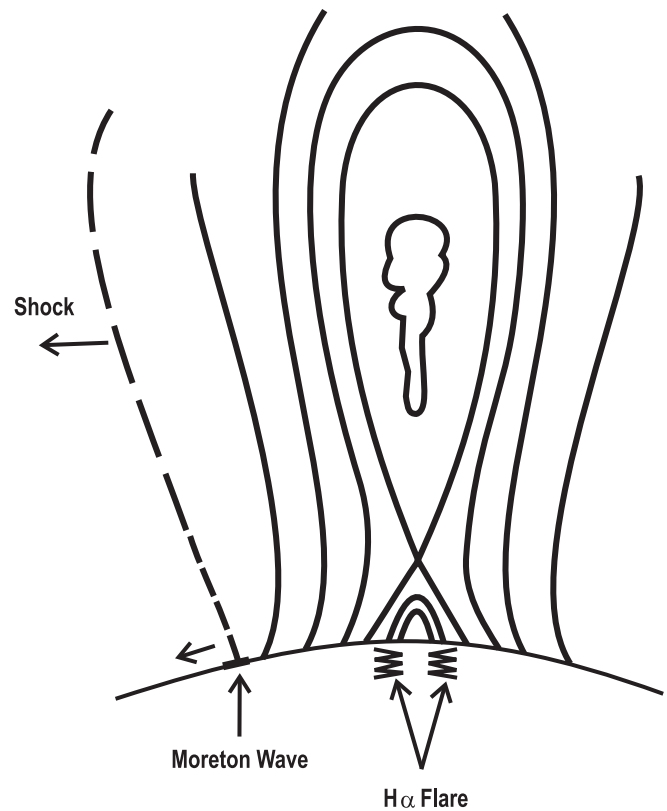

Figure 17. Cartoon showing our conception of how the expanding flank of a CME drives a shock wave laterally across the solar surface. Following the Uchida's (1968) model, the "sweeping skirt" of the radio type II coronal shock gives rise to a Moreton wave.

Figure 10) will need to be verified using events simultaneously observed with a magnetograph and a coronagraph. It seems reasonable, however, since it closely parallels the finding of Zhang et al. (2001) that the impulsive acceleration phase of CMEs coincides well with the soft X-ray flare rise phase. In this case, however, the connection to the magnetic field, generally assumed to be the source of free energy for solar activity, is more direct. This suggestion also finds support from a recent paper by Temmer et al. (2010) which compares *RHESSI* X-ray profiles with *STEREO* observations of CMEs for three fast eruptions in 2007–2008. In each case, they showed that the onset of the main phase of CME acceleration preceded the impulsive rise of the *RHESSI* > 20 keV profile by a minute or more, as was the case for the 2006 December 6 event. Similarly, Maričić et al. (2007), using soft X-ray observations, found that the majority of the 22 cases they considered, the main phase of CME acceleration preceded the principal rise in 1–8 Å emission. Additional support for a CME driver can be inferred from Temmer et al. (2010) who noted that high cadence ultraviolet and coronagraph data permitted determinations of peak CME accelerations as high as ~ 5 km s^{-2} at altitudes much lower ($\leqslant 0.4\, R_S$) than previously assumed.

It is remarkable that the most dynamic aspect of the 2006 December 6 eruption appears to have been associated with a region of relatively weak underlying magnetic field adjacent to the principal part of AR 10930 and the 3B/X6.5 flare. Such behavior has been previously reported for Moreton waves. We note that 2 of the 12 waves analyzed by Warmuth et al. (2004b), labeled 9 and 12, formed around weak flare brightenings that were removed from main flare. We infer that in such events,

instabilities in strong field regions destabilize nearby arcades that are weakly bounded, resulting in fast CMEs capable of driving large-scale waves. Analogous behavior in which eruptions involve structures located outside of strong/complex fields and their associated flares occurs for CMEs originating in transequatorial loops. Such events have been reported by Khan & Hudson (2002) and Balasubramaniam et al. (2005).

3.2. Growing Evidence for CME Drivers of Large-scale Waves

Solar flares have been reported regularly since the establishment of the world wide flare patrol in 1934. Solar Moreton waves were discovered 25 years later in 1959 (Moreton 1960) and another 15 years would pass before the first journal article on a CME (or coronal transient as they were then called) observed from space appeared (Koomen et al. 1974). Given the close temporal and spatial relationship between flares and Moreton waves, it is not surprising that the default paradigm for the origin of Moreton waves (at least up to a decade ago) is that they result from the sudden release of energy during a flare. This long-standing advantage for a flare driver was rendered moot, however, by improved observations of CMEs. In a key study, Zhang et al. (2001) used C1 (occulting disk at 1.1 $R_\odot$) coronagraph data from LASCO to show that the rapid rise of flare soft X-ray emission CME coincided with the main acceleration phase of the CME. Zhang et al. (2004) subsequently showed that CMEs could arise in a compact source region, on an AR size scale. Cliver et al. (2004b) applied these findings to a series of six type II bursts observed in 1997 November that had been previously attributed to explosive flare heating and found in each case evidence as consistent with a CME origin as with a flare origin.

While the above studies put flare and CME drivers of waves on an equal footing, several recent papers have provided more direct support for CME drivers for large-scale waves. The UltraViolet Coronagraph Spectrometer (UVCS; Kohl et al. 1995) on *SOHO* has provided strong evidence for CME drivers. Five separate UVCS cases (Raymond et al. 2000; Mancuso et al. 2002; Ciaravella et al. 2005; Mancuso & Avetta 2008; Mancuso & Bemporad 2009) have been reported where a shock, temporally associated with a type II burst, was observed via broadening and intensity changes of UV emission lines in front of a CME. Ontiveros & Vourlidas (2009) identified faint, relatively sharp shock fronts ahead of bright CME fronts in LASCO observations for 13 of 15 fast (>1500 km s^{-1}) CMEs. Liu et al. (2009) used high-cadence coronagraph observations from *STEREO*/SECCHI to associate a CME-driven streamer deflection with a metric type II burst that was subsequently observed in the decametric–hectometric range by *STEREO*/ Waves (Bougeret et al. 2008). Gopalswamy et al. (2009b) used SECCHI observations of the low corona to determine the position of the leading edge of CMEs at the onset of type II bursts observed from 2007 January to 2008 February. The typical height of ∼1.5 $R_\odot$ they deduced corresponds to the height at which the corona has a minimum Alfvén speed, consistent with a CME driver of type II shocks. Veronig et al. (2008) used SECCHI observations to suggest that an EUV wave on 2007 May 19 was a fast-mode wave initially driven by the expanding flanks of a CME. The associated *GOES* B9.5 flare peaked too late to account for wave initiation.

In other recent studies on wave origins, Patsourakos & Vourlidas (2009) and Kienreich et al. (2009) attributed a wave observed by SECCHI/EUVI that was associated with a B2.3 flare to a CME observed by the SECCHI/COR1 (inner) coronagraph. In each of these cases, the authors argued that the EUV wave was a true fast-mode MHD wave rather than a "footprint" or a low coronal extension of a CME. Patsourakos et al. (2009) used high-cadence EUVI 171 Å images and COR1 (Thompson et al. 2003) observations to associate an EUV wave with expanding loops (that evolved into a CME). The EUV wave was associated with a B1.4 flare. Patsourakos et al. noted that "The wave first appears at the AR [active region] periphery when an abrupt jump of the expanding loops occurs within an interval of 2.5 minutes and before the first flare signature." In a study involving a Moreton wave, Muhr et al. (2010) inferred separate ignition centers on opposite sides of the responsible AR for the energetic (X17) event on 2003 October 28. They interpreted this behavior in terms of an event driven by expansion of the ends of an erupting flux rope rather than in terms of explosive heating by the flare. A similar event was reported by Balasubramaniam et al. (2007) for the same AR, on 2003 October 29. Both Muhr et al. (2010) and Veronig et al. (2008) used timing relationships similar to that in Figure 6 (with wave onset in each case preceding the peak of hard X-ray emission by ∼0.5 minutes) to argue against flare drivers in the waves they investigated. In fact, in the 2003 October 28 event, the Moreton wave is observed prior to any significant increase in >150 keV emission (Figure 8 in Muhr et al. 2010).

There are four recent results, all based on pre-STEREO data, that are somewhat discordant with the studies listed above. Magdalenič et al. (2008) used radio images and EIT and LASCO C1 and C2 observations to show that the main CME acceleration phase in an event on 1996 December 24 lagged behind a type II burst that occurred close to the peak of a C2.1 flare. They concluded that the type II shock wave was ignited by the impulsive release of flare energy. Narukage et al. (2008) reported an unprecedented occurrence of three successive Moreton waves in association with a single M-class flare on 2005 August 3. They linked each of the three Moreton waves to a separate filament eruption and hypothesized that the filaments, rather than any associated CME (one was observed), drove the waves. From an analysis of a type II burst consisting of three separate emission patches on 1999 October 26, Kim et al. (2009) suggested that the first patch was due to a coronal shock generated by an X-ray plasma ejection while the two later patches were driven by a CME flank interacting with a high-density streamer. However, internal parts of a CME such as filament eruptions and flare ejecta are unlikely candidates to drive Moreton waves, because they are moving slower than the CME in which they are encased (Cliver 1999). Finally, Warmuth (2010) has discussed Moreton waves of 2003 November 3 (Vršnak et al. 2006; cf. Dauphin et al. 2006) and 1998 August 19 in which the CME flank was initially observed to be propagating ahead of the wave. Warmuth concluded that "The observations are still consistent with a flare-generated pressure pulse or with a perturbation that is only initially driven—by a CME, structures within a CME or small-scale ejecta—and then continues as a freely-propagating wave shock."

Recent statistical studies provide indirect support for CME drivers of large-scale waves, by arguing against flare drivers. Chen (2006) and Gopalswamy et al. (2008) examined samples of energetic (M- and X-class) flares that lacked CMEs for evidence of associated EIT waves and type II bursts, respectively.). Such flares should have strong pressure pulses in their loops and would thus be good candidates to give rise to large-scale waves

under the flare hypothesis, but none of the 26 independent cases (13 X-class and 13 M-class) had such associated waves. These results indicate that a pressure pulse, in itself, is an insufficient condition for wave formation. These two studies complement the work of Cliver et al. (2005) which found that ∼40% of "high-quality" EIT waves observed from 1997 March to 1998 June were associated with small solar flares below C-class. The probability of a B-class flare being associated with an EIT wave during this period was ∼1%, implying the need for a special condition (Roberts 1959; Cliver et al. 1999) for wave association. Following Biesecker et al. (2002) who found a strong association between EIT waves and CMEs, Cliver et al. (2005) concluded that the essential ingredient for wave formation was a CME.

To summarize, given

1. the well-documented examples of association of large-scale waves with B-class eruptive flares and the absence of such waves for M- and X-class flares that lack CMEs;
2. the recent cases listed above in which high-cadence observations from SECCHI were used to link type II bursts and EUV waves to CME drivers, and
3. the evidence presented here, and by Muhr et al. (2010), for CME drivers of Moreton waves associated with intense flares,

we conclude that CMEs are the dominant, if not sole, drivers of large-scale waves.

REFERENCES

Anwar, B., Acton, L. W., Hudson, H. S., Makita, M., McClymont, A. N., & Tsuneta, S. 1993, Sol. Phys., 147, 287

Athay, R. G., & Moreton, G. E. 1961, ApJ, 133, 935

Attrill, G. D. R., Engell, A. J., Wills-Davey, M. J., Grigis, P., & Testa, P. 2009, ApJ, 704, 1296

Attrill, G. D. R., Harra, L. K., van Driel-Gesztelyi, L., & Démoulin, P. 2007, ApJ, 656, L101

Balasubramaniam, K. S., Pevtsov, A. A., & Neidig, D. F. 2007, ApJ, 658, 1372

Balasubramaniam, K. S., Pevtsov, A. A., Neidig, D. F., Cliver, E. W., Thompson, B. J., Young, C. A., Martin, S. F., & Kiplinger, A. 2005, ApJ, 630, 1160

Biesecker, D. A., Myers, D. C., Thompson, B. J., Hammer, D. M., & Vourlidas, A. 2002, ApJ, 569, 1009

Bougeret, J.-L., et al. 1995, Space Sci. Rev., 71, 231

Bougeret, J.-L., et al. 2008, Space Sci. Rev., 136, 487

Brueckner, G. E., et al. 1995, Sol. Phys., 162, 357

Cane, H. V., & Erickson, W. C. 2005, ApJ, 623, 1180

Cane, H. V., Sheeley, N. R., Jr., & Howard, R. A. 1987, J. Geophys. Res., 92, 9869

Chen, P. F. 2006, ApJ, 641, L153

Chen, P. F. 2009, ApJ, 698, L112

Chen, P. F., Fang, C., & Shibata, K. 2005, ApJ, 622, 1202

Chen, P. F., Wu, S. T., Shibata, K., & Fang, C. 2002, ApJ, 572, L99

Ciaravella, A., Raymond, J. C., Kahler, S. W., Vourlidas, A., & Li, J. 2005, ApJ, 621, 1121

Cliver, E. W. 1999, J. Geophys. Res., 104, 4743

Cliver, E. W., Kahler, S. W., & Reames, D. V. 2004a, ApJ, 605, 902

Cliver, E. W., Laurenza, M., Storini, M., & Thompson, B. J. 2005, ApJ, 631, 604

Cliver, E. W., Nitta, N. V., Thompson, B. J., & Zhang, J. 2004b, Sol. Phys., 225, 105

Cliver, E. W., Webb, D. F., & Howard, R. A. 1999, Sol. Phys., 187, 89

Cohen, O., Attrill, G. D. R., Manchester, W. B., IV, & Wills-Davey, M. J. 2009, ApJ, 705, 587

Culhane, J. L., et al. 2007, Sol. Phys., 243, 19

Czaykowska, A., De Pontieu, B., Alexander, D., & Rank, G. 1999, ApJ, 521, L75

Dai, Y., Auchère, F., Vial, J.-C., Tang, Y. H., & Zong, W. G. 2010, ApJ, 708, 913

Dauphin, C., Vilmer, N., & Krucker, S. 2006, A&A, 455, 339

Delannée, C. 2000, ApJ, 545, 512

Delannée, C., & Aulanier, G. 1999, Sol. Phys., 190, 107

Delannée, C., Török, T., Aulanier, G., & Hochedez, J.-F. 2008, Sol. Phys., 247, 123

Dere, K. P., et al. 1997, Solar Phys., 175, 601

Dodson, H. W., & Hedeman, E. R. 1964, in Proc. AAS-NASA Symp., Physics of Solar Flares, ed. W. N. Hess (Washington, DC: NASA), 15

Dodson, H. W., & Hedeman, E. R. 1968, Sol. Phys., 4, 229

Forbes, T. 2000, J. Geophys. Res., 105, 23153

Gilbert, H. R., Daou, A. G., Young, D., Tripathi, D., & Alexander, D. 2008, ApJ, 685, 629

Gilbert, H. R., & Holzer, T. E. 2004, ApJ, 610, 572

Gopalswamy, N., Akiyama, S., & Yashiro, S. 2008, in Proc. IAU. Symp. 257, Universal Heliophysical Processes, ed. N. Gopalswamy & D. F. Webb (Cambridge: Cambridge Univ. Press), 283

Gopalswamy, N., et al. 1998, J. Geophys. Res., 103, 307

Gopalswamy, N., et al. 1999, J. Geophys. Res., 104, 4749

Gopalswamy, N., et al. 2000, Geophys. Res. Lett., 27, 1427

Gopalswamy, N., et al. 2009a, ApJ, 691, L123

Gopalswamy, N., et al. 2009b, Sol. Phys., 259, 227

Handy, B. N., et al. 1999, Sol. Phys., 187, 229

Harra, L. K., & Sterling, A. C. 2003, ApJ, 587, 429

Harra, L. K., Hara, H., Imada, S., Young, P. R., Williams, D. R., Sterling, A. C., Korendyke, C., & Attrill, G. D. R. 2007, PASJ, 59, S801

Harvey, K. L. 1971, Sol. Phys., 16, 423

Harvey, K. L., Martin, S. F., & Riddle, A. C. 1974, Sol. Phys., 36, 151

Harvey, K. L., & Recely, F. 1984, Sol. Phys., 91, 127

Harvey, J., et al. 1988, in Seismology of the Sun and Sunlike Stars, ed. E. J. Rolfe, ESA SP-286 (Noordwijk: ESA), 203

Howard, R. A., et al. 2008, Space Sci. Rev., 136, 67

Hudson, H. S., Acton, L. W., Hirayama, T., & Uchida, Y. 1992, PASJ, 44, L77

Hudson, H. S., Fisher, G. H., & Welsch, B. T. 2008, in ASP Conf. Ser. 383, Subsurface and Atmospheric Influences on Solar Activity, ed. R. Howe, R. W. Komm, K. S. Balasubramaniam, & G. J. D. Petrie (San Francisco, CA: ASP), 221

Hudson, H. S., Khan, J. I., Lemen, J. R., Nitta, N. V., & Uchida, Y. 2003, Sol. Phys., 212, 121

Imada, S., Hara, H., Watanabe, T., Kamio, S., Asai, A., Matsuzaki, K., Harra, L. K., & Mariska, J. T. 2007, PASJ, 59, S793

Isobe, H., et al. 2007, PASJ, 59(SP3), S807

Kahler, S. W. 1982, J. Geophys. Res., 87, 3439

Kahler, S. W., Sheeley, N. R., Jr., Howard, R. A., Michels, D. J., Koomen, M. J., McGuire, R. E., von Rosenvinge, T. T., & Reames, D. V. 1984, J. Geophys. Res., 89, 9683

Khan, J. I., & Aurass, H. 2002, A&A, 383, 1018

Khan, J. I., & Hudson, H. S. 2002, Geophys. Res. Lett., 27, 1083

Kienreich, I. W., Temmer, M., & Veronig, A. M. 2009, ApJ, 703, L118

Kim, Y.-H., Bong, S.-C., Park, Y.-D., Cho, K.-S., & Moon, Y.-J. 2009, ApJ, 705, 1721

Kohl, J. L., et al. 1995, Sol. Phys., 162, 313

Koomen, M., Howard, R., Hansen, R., & Hansen, S. 1974, Sol. Phys., 34, 447

Lin, R. P., et al. 2002, Sol. Phys., 210, 3
Liu, Y., Luhmann, J. G., Bale, S. D., & Lin, R. P. 2009, ApJ, 691, L151
Long, D. M., Gallagher, P. T., McAteer, R. T. J., & Bloomfield, D. S. 2008, ApJ, 680, L81
Ma, S., et al. 2009, ApJ, 707, 503
Magdalenić, J., Vršnak, B., Pohjolainen, S., Temmer, M., Aurass, H., & Lehtinen, N. J. 2008, Sol. Phys., 253, 305
Mancuso, S., & Avetta, D. 2008, ApJ, 677, 683
Mancuso, S., & Bemporad, A. 2009, Adv. Space Res., 44, 451
Mancuso, S., Raymond, J. C., Kohl, J., Ko, Y.-K., Uzzo, M., & Wu, R. 2002, A&A, 383, 267
Maričić, D., Vršnak, B., Stanger, A., Veronig, A. M., Temmer, M., & Roša, D. 2007, Sol. Phys., 241, 99
Moreton, G. E. 1960, AJ, 65, 494
Moreton, G. E. 1961, Sky Telescope, 21, 145
Moreton, G. E. 1964, AJ, 69, 145
Moreton, G. E., & Ramsey, H. E. 1960, PASP, 72, 357
Muhr, M., Temmer, M., Veronig, A., Vršnak, B., & Hanslmeier, A. 2008, Cent. Eur. Astrophys. Bull., 32, 79
Muhr, N., Vršnak, B., Temmer, M., Veronig, A. M., & Magdalenić, J. 2010, ApJ, 708, 1639
Narukage, N., Hudson, H. S., Morimoto, T., Akiyama, S., Kitai, R., Kurokawa, H., & Shibata, K. 2002, ApJ, 572, L109
Narukage, N., Ishii, T. T., Nagata, S., UeNo, S., Kitai, R., Kurokawa, H., Akioka, M., & Shibata, K. 2008, ApJ, 684, L45
Neidig, D. F., Švestka, Z., Cliver, E. W., Airapetian, V., & Henry, T. W. 1997, Sol. Phys., 170, 321
Neidig, D., et al. 1998, in ASP Conf. Ser. 140, Synoptic Solar Physics, ed. K. S. Balasubramaniam, J. Harvey, & D. Rabin (San Francisco, CA: ASP), 519
Neupert, W. M. 1989, ApJ, 344, 504
Ontiveros, V., & Vourlidas, A. 2009, ApJ, 693, 267
Patsourakos, S., & Vourlidas, A. 2009, ApJ, 700, L182
Patsourakos, S., Vourlidas, A., Wang, Y.-M., Stenborg, G., & Thernisien, A. 2009, Sol. Phys., 259, 49
Payne-Scott, R., Yabsley, D. E., & Bolton, J. G. 1947, Nature, 160, 256
Petrie, G. J. D., & Sudol, J. J. 2010, ApJ, submitted
Pick, M., Malherebe, J.-M., Kerdraon, M., & Maia, D. J. F. 2005, ApJ, 631, L97
Ramsey, H. E., & Smith, S. F. 1966, AJ, 71, 197
Raymond, J. C., et al. 2000, Geophys. Res. Lett., 27, 1439
Roberts, J. A. 1959, Aust. J. Phys., 12, 327
Scherrer, P. H., et al. 1995, Sol. Phys., 162, 129
Sheeley, N. R., Jr., Howard, R. A., Koomen, M. J., Michels, D. J., Schwenn, R., Mühlhäuser, K. H., & Rosenbauer, H. 1985, J. Geophys. Res., 90, 163
Smith, S. F., & Harvey, K. L. 1971, in Physics of the Solar Corona, ed. C. J. Macris (Dordrecht: Reidel), 156
Sudol, J. J., & Harvey, J. W. 2005, ApJ, 635, 647
Temmer, M., Veronig, A. M., Kontar, E. P., Krucker, S., & Vršnak, B. 2010, ApJ, 712, 1410
Temmer, M., Veronig, A., Vršnak, B., Rybák, J., Gömöry, P., Stoiser, S., & Maričić, D. 2008, ApJ, 673, L95
Temmer, M., Vršnak, B., Žic, T., & Veronig, A. M. 2009, ApJ, 702, 1343
Thompson, B. J., Plunkett, S. P., Gurman, J. B., Newmark, J. S., St. Cyr, O. C., & Michels, D. J. 1998, Geophys. Res. Lett., 25, 2465
Thompson, B. J., et al. 1999, ApJ, 517, L151
Thompson, W. T., et al. 2003, Proc. SPIE, 4583, 1
Tsuneta, S., et al. 2008, Sol. Phys., 249, 167
Uchida, Y. 1968, Sol. Phys., 4, 30
Uchida, Y. 1973, NASA Symp. on High Energy Phenomena on the Sun, ed. R. Ramaty & R. G. Stone (Greenbelt, MD: NASA), 577
Uchida, Y. 1974a, in IAU Symp. 57, Coronal Disturbances, ed. G. Newkirk (Dordrecht: Reidel), 383
Uchida, Y. 1974b, Sol. Phys., 39, 431
Uchida, Y., Altschuler, M. D., & Newkirk, G. A. 1973, Sol. Phys., 28, 495
Veronig, A. M., Muhr, N., Kienreich, I. W., Temmer, M., & Vršnak, B. 2010, ApJ, 716, L57
Veronig, A. M., Temmer, M., & Vršnak, B. 2008, ApJ, 681, L113
Veronig, A. M., Temmer, M., Vršnak, B., & Thalmann, J. K. 2006, ApJ, 647, 1466
Vršnak, B. 2005, EOS Trans., 86, 112
Vršnak, B., & Cliver, E. W. 2008, Sol. Phys., 253, 215
Vršnak, B., Warmuth, A., Brajša, R., & Hanslmeier, A. 2002, A&A, 394, 299
Vršnak, B., Warmuth, A., Temmer, M., Veronig, A., Magdalenić, J., Hillaris, A., & Karlický, M. 2006, A&A, 448, 739
Wang, H., Shen, C., & Lin, J. 2009, ApJ, 700, 1716
Wang, H.-M. 2009, Res. Astron. Astrophys., 9, 12
Wang, Y., & Zhang, J. 2007, ApJ, 665, 1428
Warmuth, A. 2007, The High Energy Solar Corona: Waves, Eruptions, Particles, Lecture Notes in Physics 725 (Berlin: Springer), 107
Warmuth, A. 2010, Adv. Space Res., 45(4), 527
Warmuth, A., Mann, G., & Aurass, H. 2005, ApJ, 626, L121
Warmuth, A., Vršnak, B., Magdalenić, J., Hanslmeier, A., & Otruba, W. 2004a, A&A, 418, 1101
Warmuth, A., Vršnak, B., Magdalenić, J., Hanslmeier, A., & Otruba, W. 2004b, A&A, 418, 1117
White, S. M. 2007, Asian J. Phys., 16, 189
White, S. M., & Thompson, B. J. 2005, ApJ, 620, L63
Wild, J. P., & McCready, L. L. 1950, Aust. J. Sci. Res., A3, 387
Wills-Davey, M. J., & Attrill, G. D. R. 2009, Space Sci. Rev., 149, 325
Wuelser, J. P., et al. 2004, Proc. SPIE, 5171, 111
Yang, H. Q., & Chen, P. F. 2010, Sol. Phys., in press
Yashiro, S., Gopalswamy, N., Akiyama, S., Michalek, G., & Howard, R. A. 2005, J. Geophys. Res., 110, A12S05
Zhang, J., & Dere, K. P. 2006, ApJ, 649, 1100
Zhang, J., Dere, K. P., Howard, R. A., Kundu, M. R., & White, S. M. 2001, ApJ, 559, 452
Zhang, J., Dere, K. P., Howard, R. A., & Vourlidas, A. 2004, ApJ, 604, 420
Zhukov, A. N., & Auchére, F. 2004, A&A, 427, 705
Zhukov, A. N., Rodriguez, L., & de Patoul, J. 2009, Sol. Phys., 259, 73